Posted: June 18, 2025

# Laminar flow simulation in square cross-section duct using OpenFOAM

Hector Espinoza-Roman[1,*]

[1]Fundacion Universitaria Antonio de Arevalo UNITECNAR, Direccion de Investigacion e Innovacion, Calle 49A 31-45, 130004 Cartagena de Indias, Colombia; ORCID: 0000-0002-2861-2442

[*]Corresponding author: hector.espinoza@unitecnar.edu.co

**Abstract**

This case study is motivated by the need of having a very simple case that can be simulated in a computational fluid dynamics software. The requirement of the flow case is to have a known exact solution in order to compare with the simulation results. The objective is to simulate the flow using OpenFOAM and to compare the results of the simulation with the exact solution. The simulation was done following the classical computational fluid dynamics workflow: geometry generation, boundary condition imposition, meshing, solving and post-processing. The simulation was performed for three different meshes. Finally, the computational results were compared with the analytical solution. The simulation yielded the velocity profile for fully developed flow, the pressure profile in the longitudinal direction, and the pressure variation per unit length. The results are in agreement with the exact solution of the flow. Therefore, OpenFOAM was able to simulate accurately the flow in terms of velocity and pressure.

## 1 Introduction

While OpenFOAM has been widely used for fluid dynamics simulations [Huang et al., 2022, Zhang et al., 2024], a rigorous comparison between its numerical results and established analytical solutions for laminar flow in a square cross-section straight duct remains limited. This study addresses this gap by performing a detailed validation of OpenFOAM's capabilities, presenting a direct comparison with a known exact solution. To the best of the authors' knowledge, such a comprehensive validation for this specific flow scenario has not been previously presented.

This case study is motivated by the need of having a very simple case that can be simulated in a Computational Fluid Dynamics (CFD) software with a known solution to compare with the simulation results. Several tutorial cases exist for many CFD software packages [Mahmudah et al., 2023], however, for the case of OpenFOAM software [Greenshields, 2023], the tutorials included in its documentation have complex geometries and often a mix of complex models and physics. Those tutorials can be difficult to understand for students from a first course in CFD. Additionally, the tutorials rarely include a comparison with a known solution.

This study attempts to validate the working hypothesis: the application of OpenFOAM in simulating laminar flow in a square cross-section duct will provide accurate results that align with theoretical predictions for a fine enough mesh.

This work has two objectives. The first one is to simulate the laminar flow in a square cross-section duct using OpenFOAM. The second one is to compare the results obtained from the OpenFOAM simulation with the exact solution of the problem (verification and validation). The comparison is done in terms of pressure, velocity and friction factor.

This article is organized as follows: first, a literature review on the topic is presented. Then, the methodology is described. Next, the results obtained are shown. Afterwards, a discussion of the results is performed. Finally, the conclusions are drawn.

## 2 Literature Review

Flow in ducts and pipes is a common phenomenon in various industrial applications across mechanical, chemical, and civil engineering. This flow is often referred to as internal flow, Poiseuille flow, or Hagen-Poiseuille flow. The Newtonian incompressible fluid model is frequently used to simulate common fluids such as water [Bar-Meir, 2023].

Several factors influence the flow in pipes, including the fluid's density, the fluid's dynamic viscosity, the shape and size of the pipe cross-section, the roughness of the pipe material, and the pipe's length [Bar-Meir, 2023, Çengel and Cimbala, 2018, Shah and London, 1978]. The analysis of flow in pipes can be approached in several ways: analytical approach [Spiga and Morino, 1994, Moharana and Khandekar, 2013, Wheeler and Wissler, 1965, El-Genk and Pourghasemi, 2019], experimental approach [Xu et al., 2000, Li et al., 2019], and computational approach [Barmak et al., 2024, El-Genk and Pourghasemi, 2019, Li et al., 2019, Syrjälä, 1995].

The analytical approach involves solving the flow equations exactly to obtain an analytical solution. This method provides a deep understanding of the phenomenon and yields an exact solution [El-Genk and Pourghasemi, 2019]. However, its application is limited to simple geometries or straightforward cases where an exact solution can be found. For the case of square duct hydrodynamics, Moharana and Khandekar [2013] developed a generalized formulation based on collocation points to determine the pressure drop.

The experimental approach involves measuring values of interest by conducting laboratory experiments [Orozco et al., 2022]. This method has the advantage of being as realistic as possible. However, the challenges of this approach lie in the cost of each experiment and the measurement instruments.

The computational approach involves solving the flow equations approximately using a computer [González-Estrada et al., 2022]. The obtained solution becomes increasingly accurate as more elements are used in the computational mesh. This method can be applied to various geometries and to steady or transient states [Rodríguez-Díaz et al., 2023, Lain and Caballero, 2023]. The challenges of this approach include having a sufficiently verified and validated simulation software with the necessary physics implemented [Ashton and Skaperdas, 2019, Noriega et al., 2018].

CFD has been used extensively to model a wide variety of problems ranging from laminar to turbulent flow, internal and external flow, incompressible and compressible flow; and, two- and three-dimensional geometries. Additionally, several CFD software have been utilized such as OpenFOAM, Star-CCM+, ANSYS FLUENT, among others. Furthermore, CFD simulations are often compared to experimental results, analytical solutions or more advanced simulations (such as Direct Numerical Simulations) in order to check their accuracy [Neeraj et al., 2023, Quingatuña-Cali et al., 2022, Shingala et al., 2022, Lumentut and Friswell, 2022]. In this work, we compare the CFD result to an analytical solution.

In this article, we will use the computational approach using OpenFOAM v11 [Greenshields, 2023]. OpenFOAM is an open-source CFD software that implements the finite volume method under the GNU GPL license (GNU General Public License). It is essential for open science in the field of computational simulation the use of open-source software [Reina-Rozo and Medina-Cardona, 2021]. Furthermore, within the realm of CFD, the monetary cost associated with commercial software packages poses a significant challenge. However, this is where open-source software comes into play [Liu et al., 2020].

An incompressible (constant density), single-phase, isothermal flow in steady state (also known as a stationary state) can be described with the velocity vector $\boldsymbol{v}(\boldsymbol{x}) = (u(\boldsymbol{x}), v(\boldsymbol{x}), w(\boldsymbol{x}))$ and the pressure $p(\boldsymbol{x})$, where $\boldsymbol{x} = (x, y, z)$ is any point in space. Velocity and pressure must satisfy the Navier-Stokes equations.

The flow in ducts and pipes of arbitrary cross section can be characterized by the hydraulic diameter $D_\mathrm{h}$ defined as

$$D_\mathrm{h} = \frac{4A}{p_\mathrm{c}}, \tag{1}$$

where $A$ is the cross-section area and $p_\mathrm{c}$ is the perimeter of the cross-section. For square cross-section ducts of side $a$, the hydraulic diameter is

$$D_\mathrm{h} = a. \tag{2}$$

The average velocity $V$ of the fluid across an arbitrary shape cross-section of area $A$ is defined as

$$V = \frac{1}{A}\int_A \boldsymbol{v}\cdot\boldsymbol{n}\mathrm{d}A, \tag{3}$$

where $\mathrm{d}A$ is the area differential, $\boldsymbol{n}$ is the normal unit vector to the cross-section and the integral represents a surface integral.

The flow rate of a fluid can be quantified as discharge or volumetric flow rate $Q$ defined as

$$Q = VA. \tag{4}$$

Additionally, the flow regime is characterized by the Reynolds Number Re defined as

$$\mathrm{Re} = \frac{\rho V D_\mathrm{h}}{\mu}, \tag{5}$$

where $\rho$ is the density of the fluid and $\mu$ is the dynamic viscosity of the fluid. The Reynolds number allows classifying the flow as laminar flow, transitional flow and turbulent flow. For pipe flow, the flow is laminar when $\mathrm{Re} < 2300$ [Çengel and Cimbala, 2018]. The fluid viscosity can be expressed as kinematic viscosity $\nu$ defined as

$$\nu = \frac{\mu}{\rho}. \tag{6}$$

The pressure as well can be expressed as kinematic pressure $P$ defined as

$$P = \frac{p}{\rho}. \tag{7}$$

Another important aspect of pipe flow is the concept of developing flow and fully developed flow characteristics. A flow is said to be fully developed when its velocity profile remains constant in the direction of flow. On the other hand, the flow is developing when the velocity profile changes in the flow direction and can be quantified by the entrance length $L_\mathrm{e}$ defined for laminar flow as

$$L_\mathrm{e} = 0.05\mathrm{Re}D_\mathrm{h}. \tag{8}$$

Pressure drop in a pipe [Bar-Meir, 2023] can be calculated as

$$\Delta p = f\frac{L}{D_\mathrm{h}}\rho\frac{V^2}{2}, \tag{9}$$

where $L$ is the pipe length and $f$ is the Darcy-Weisbach friction factor. Note that some definitions use the Fanning friction factor $(f/4)$ such as Syrjälä [1995]. In this work we use the Darcy-Weisbach friction factor and we refer to it simply as friction factor from now on. The friction factor is found in graphical form in the Moody diagram. For laminar flow analysis in square cross-section ducts [Shah and London, 1978] it holds

$$\mathrm{Po} = f\mathrm{Re} = 56.91, \tag{10}$$

where Po is the so called Poiseuille number [Moharana and Khandekar, 2013].

The geometry of the duct is presented in Fig. 1.

The velocity profile for fully developed laminar flow in square-cross section ducts [Spiga and Morino, 1994] can be expressed as

$$w(\xi,\eta) = 16\frac{C}{\pi^4}\sum_{\substack{n\\ \mathrm{odd}}}^{\infty}\sum_{\substack{m\\ \mathrm{odd}}}^{\infty}\frac{\sin(n\pi\xi)\sin(m\pi\eta)}{nm(n^2+m^2)}, \tag{11}$$

where $\xi = x/a$, $\eta = y/a$ and $C$ is a constant defined as

$$C = \frac{a^2}{\mu}\frac{\mathrm{d}p}{\mathrm{d}z}. \tag{12}$$

In addition, the average velocity [Spiga and Morino, 1994] can be expressed as

$$V = 64\frac{C}{\pi^6}\sum_{\substack{n\\ \mathrm{odd}}}^{\infty}\sum_{\substack{m\\ \mathrm{odd}}}^{\infty}\frac{1}{n^2m^2(n^2+m^2)}. \tag{13}$$

The ratio between maximum velocity and average velocity for square cross-section pipes [Shah and London, 1978] is

$$\frac{w_\mathrm{max}}{V} = 2.0962. \tag{14}$$

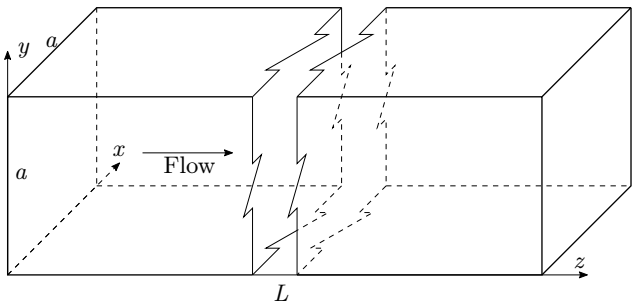


Figure 1: Geometry of the duct

# 3 Methodology

This section describes the methodology used to define the geometry, impose boundary conditions, generate the mesh, simulate the flow and visualize the results. For more details, the reader is referred to the files of the simulation. We decided to do the simulation at Re = 640 in such a way that it is not so low or so close to the 2300 limit. The intention is to always have numbers without so many decimals, non-unitary and well defined at least in the input data. The idea of having non-unitary values is that they effectively influence the results by changing their numerical value. In the results, as will be seen later, most values have many decimal places since the analytical solution has many decimal places.

The simulation presented in this article is defined by the following fixed quantities taken as constants as seen in Tab. 1: side of cross section, pipe length, average velocity, density, dynamic viscosity, volumetric flow , hydraulic diameter and Reynolds number. On the other hand, the variables that are calculated from the simulation are: velocity field, pressure field, pressure drop per unit length and maximum velocity.

Table 1: Input data and derived data

| **Data** | **Value** | **Derived Data** | **Value** |
|---|---|---|---|
| $a$ | 0.1 m | $\nu$ | 5E-4 $m^2/s$ |
| $L$ | 10 m | $D_h$ | 0.1 m |
| $V$ | 3.2 m/s | Re | 640 |
| $\rho$ | 2 $kg/m^3$ | $Q$ | 0.032 $m^3/s$ |
| $\mu$ | 0.001 Pa s | | |

## 3.1 Geometry

Fig. 1 shows the geometry of the case and its location with respect to the coordinate axes. The geometry consists of a duct of square cross section of side $a$ and length $L$ in 3D. We name that volume spatial domain. The spatial domain extends from point $(x, y, z) = (0,0,0)$ up to the point $(a, a, L)$. The spatial domain can be expressed as well as $(0, a) \times (0, a) \times (0, L)$. We took $a = 0.1$ m to have a non unitary value of the side length. Then, we take $L = 10$ m to have a relation $L/D_h = 100$ in order to be far from the length of developing flow which, according to Eq. (8) is $L_e/D_h = 32$.

Due to the geometric simplicity of the spatial domain, we use blockMesh to generate the geometry, impose boundary conditions and generate the computational grid, all in one step [Bibin and Jayakumar, 2020]. We needed only one block due to the simplicity of the geometry.

## 3.2 Boundary Conditions

Tab. 2 summarizes the boundary conditions and Fig. 2 shows the boundary conditions [Riaz et al., 2022]. In the inlet we specified a fixed flow rate, so we do not impose a velocity profile and hence, the

velocity profile appears as a result of the simulation. Additionally, we used the extrapolateProfile OpenFOAM option to attain fully developed flow rapidly. This modifier does not affect the results since we are only interested in the fully developed velocity profile. In the outlet we used a typical condition for outlets in internal flow which consists of fixed pressure equal to zero (fixedValue) and velocity is left free. Finally, in the four walls, we used the non-slip boundary condition since we are dealing with viscous flow.

Table 2: Boundary Conditions

| **ID** | **Velocity** | **Pressure** |
|---|---|---|
| inlet | flowRateInletVelocity | zeroGradient |
| outlet | inletOutlet | fixedValue |
| wall | noSlip | zeroGradient |

The extrapolateProfile boundary condition extrapolates the velocity profile of the interior to the boundary. It attempts to impose a fully developed flow boundary condition.

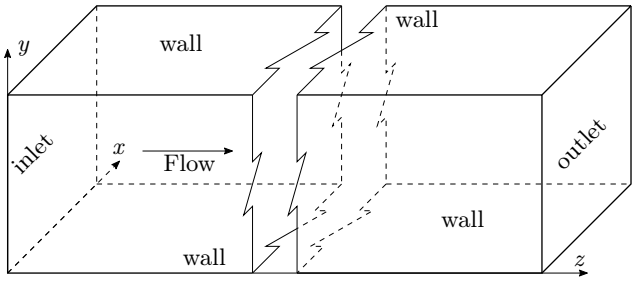


Figure 2: Boundary Conditions

## 3.3 Mesh

The mesh is composed by hexahedral elements [Liu et al., 2024]. We used the same number of elements in $x$ and $y$ direction ($N_x = N_y$) as the cross-section is square and we expect a symmetric solution. Additionally, we used an even number of elements to have a node in the middle of the cross-section to contribute to the symmetry of the flow. We used $N_x = 10$, 20 and 40, denoted as Mesh10, Mesh20 and Mesh40 to have three meshes with a progressive refinement with a factor of 2 to be able to perform a mesh convergence study and mesh sensitivity analysis. Fig. 3 shows an example mesh for $N_x = 10$. In addition, we used a uniform element distribution in $x$ and $y$ direction because the intention is to have a simple spatial resolution and not finding the optimal element distribution. As we seek a fully developed flow solution, it was desirable to use a small quantity of elements in the $z$ direction (small $N_z$) because the simulation is steady-state. However, we do not use a small quantity of elements to avoid errors introduced by the inlet and outlet boundary conditions. Hence, we use $N_z = 100$. The aspect ratio of elements ranges from 10 in Mesh10 to 40 in Mesh40. Since the exact solution does not change in the $z$ direction, the high aspect ratio of the elements is not an issue. Fig. 4 shows an example of the mesh for $N_x = 10$ in plane $yz$ where 10 elements in $y$ direction and 2 elements in $z$ direction are shown. Fig. 5 shows a partial view of the mesh in 3D for $N_x = 10$.

We used blockMesh to generate the mesh. For instance, the mesh obtained for $N_x = 10$ has 12221 nodes and 10000 hexahedral elements. Tab. 3 summarizes the main characteristics of the meshes.

## 3.4 Computational Solution

To solve the flow problem, we used the incompressibleFluid solver [Greenshields, 2023] as the flow is incompressible, viscous, laminar and steady state. Tab. 4 shows the numerical schemes used to solve the problem. All the schemes are the usual ones used for the incompressibleFluid tutorials

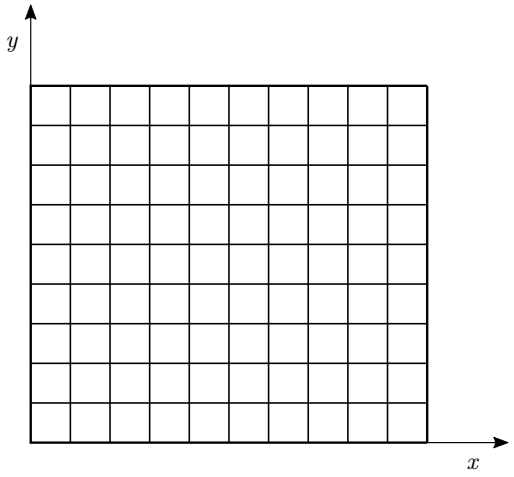


Figure 3: Example of mesh in plane $xy$ for $N_x = 10$

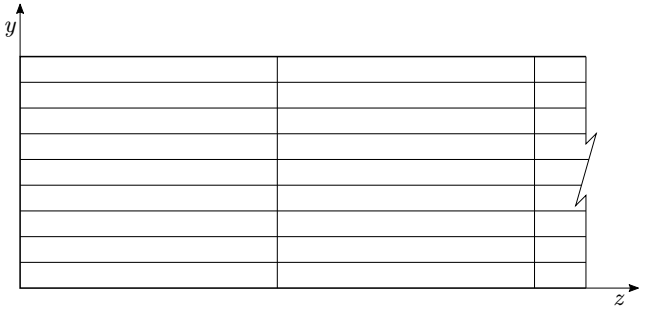


Figure 4: Example of mesh in plane $zy$ for $N_x = 10$

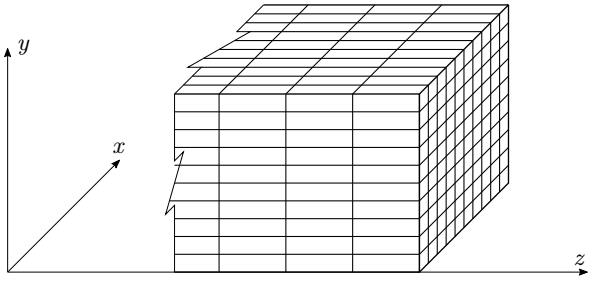


Figure 5: Partial view of the mesh in 3D for $N_x = 10$

Table 3: Meshes used for the simulation

| **Mesh** | $N_x$ | **Elements** | **Nodes** |
|---|---|---|---|
| Mesh10 | 10 | 10000 | 12221 |
| Mesh20 | 20 | 40000 | 44541 |
| Mesh40 | 40 | 160000 | 169781 |

(i.e. movingCone) with the exception of div(phi,U) where we use the more robust and stable Gauss upwind scheme.

Table 4: Numerical Schemes

| Scheme | Type |
|---|---|
| ddtSchemes | steadyState |
| gradSchemes | Gauss linear |
| div(phi,U) | Gauss upwind |
| laplacianSchemes | Gauss linear corrected |
| interpolationSchemes | linear |
| snGradSchemes | corrected |

### 3.5 Computational Resources

The computational resources used to perform the simulation can be summarized as a laptop computer with operating system Ubuntu 22.04 64bits. The computer has an Intel Core i5-8250U processor with 16GB of RAM DDR4 2400MHz dual-channel (8GB + 8GB) and a Solid State Drive disk WD Blue 500GB connected through PCIe.

### 3.6 Additional Software Resources

The graphs were done using gnuplot [Williams and Kelley, 2022]. Additionally, we used Python [Downey, 2015] with NumPy [NumPy Community, 2021] to manipulate the results generated by OpenFOAM and to generate the analytical solution. Furthermore, we used TeX Live [Berry, 2023] and Geany [Troger et al., 2023] to generate the manuscript.

## 4 Results

The flow was resolved in all the computational domain. This is, we obtained velocity and pressure everywhere. In order to be able to compare the computational results with the analytical solution, we selected three main results: variation of pressure in the axial direction ($z$-axis) and two velocity profiles from two different cuts.

### 4.1 Pressure

Fig. 6 shows the kinematic pressure along the axial direction in the centerline of the pipe.

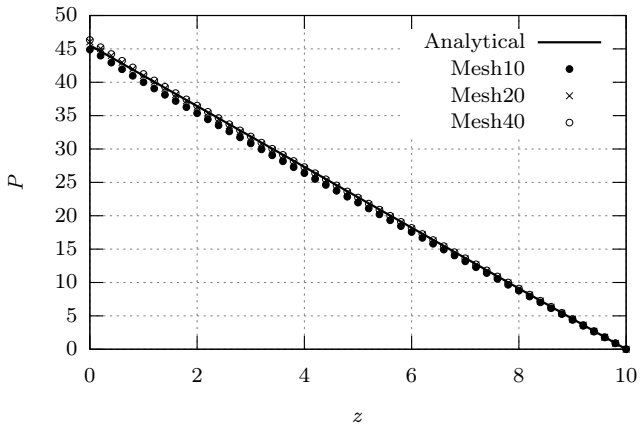


Figure 6: Comparison of $P$ vs $z$ for various meshes and analytical solution [Bar-Meir, 2023, Shah and London, 1978] for $x = y = a/2$

In order to better visualize the result, we plot the slope of the curve calculated point to point as shown in Fig. 7. The slope was calculated using a first-order finite difference scheme according to the following equation:

$$\left(\frac{\mathrm{d}P}{\mathrm{d}z}\right) = \frac{P_i - P_{i-1}}{z_i - z_{i-1}}, \quad i = 1, 2, ..., N_z \tag{15}$$

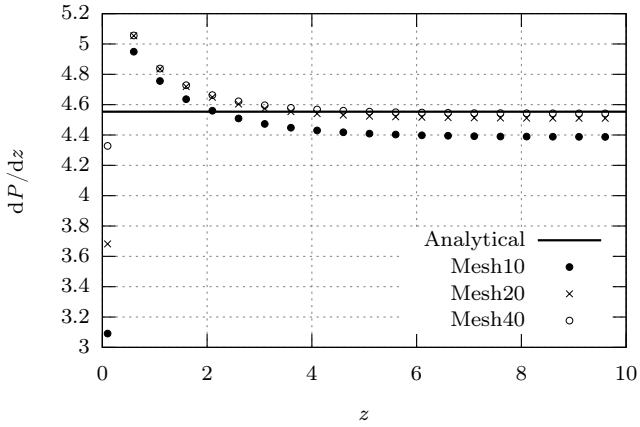


Figure 7: Comparison of $\mathrm{d}P/\mathrm{d}z$ vs $z$ for various meshes and analytical solution [Bar-Meir, 2023, Shah and London, 1978] for $x = y = a/2$

Tab. 5 shows a comparison of the values obtained for $\mathrm{d}P/\mathrm{d}z$ for different meshes.

Table 5: Comparison of $\mathrm{d}P/\mathrm{d}z$, $f$ and $\mathrm{Po} = f\mathrm{Re}$ at $z = 4/5L$

| **Mesh** | $\mathrm{d}P/\mathrm{d}z$ | $f$ | $f\mathrm{Re}$ | **Error (%)** $f\mathrm{Re}$ |
|---|---|---|---|---|
| Mesh10 | 4.3897 | 0.0857 | 54.85 | 3.62 |
| Mesh20 | 4.5113 | 0.0881 | 56.38 | 0.93 |
| Mesh40 | 4.5432 | 0.0887 | 56.77 | 0.25 |
| Analytical[a] | 4.5536 | 0.0889 | 56.91 | 0 |

[a] [Shah and London, 1978]

## 4.2 Velocity profiles

We decided to obtain the velocity profiles at $z = 4/5L$ because according to Fig. 7 it can be seen that the flow is fully developed in that coordinate. Additionally, at that coordinate we keep a distance with respect to the outlet surface. Fig. 8 shows the velocity profile for $y = a/2$ and $z = 4/5L$ and Tab. 6 shows a comparison between velocities and velocity ratios.

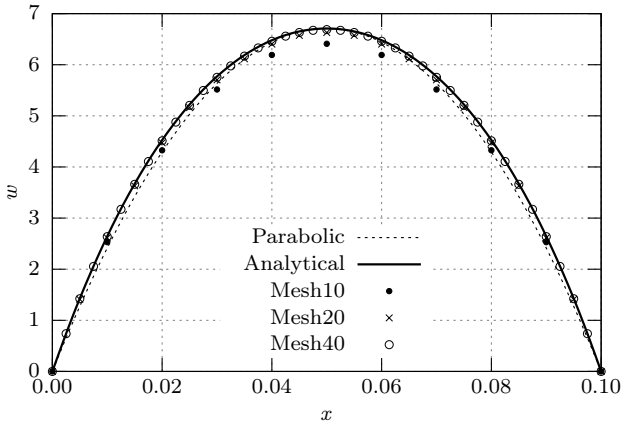


Figure 8: Comparison of velocity profiles for various meshes and analytical solution [Spiga and Morino, 1994] at $y = a/2$ and $z = 4/5L$

Fig. 9 shows another velocity profile from another cut (a diagonal cut), this time for $x = y$ at $z = 4/5L$.

Table 6: Comparison of $w_{\max}$ and $w_{\max}/V$ at $z = 4/5L$

| **Mesh** | $w_{\max}$ | $w_{\max}/V$ | **Error (%)** $w_{\max}/V$ |
|---|---|---|---|
| Mesh10 | 6.4099 | 2.0031 | 4.44 |
| Mesh20 | 6.6296 | 2.0718 | 1.16 |
| Mesh40 | 6.6874 | 2.0898 | 0.31 |
| Analytical[a] | 6.7078 | 2.0962 | 0 |

[a] Shah and London [1978]

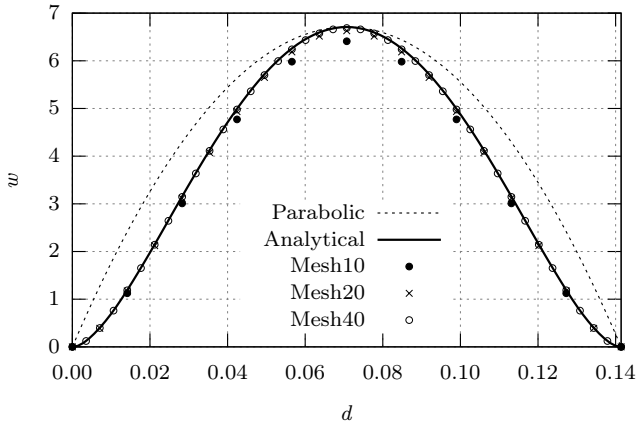


Figure 9: Comparison of velocity profiles for various meshes and analytical solution [Spiga and Morino, 1994] for $x = y$ at $z = 4/5L$. $d = \sqrt{x^2 + y^2}$

## 4.3 Calculation time and memory

Tab. 7 shows the calculation time required for each mesh and the amount of RAM memory consumed.

Table 7: Calculation time and memory

| **Mesh** | **Time (s)** | **Memory (MB)** |
|---|---|---|
| Mesh10 | 10 | 114 |
| Mesh20 | 47 | 172 |
| Mesh40 | 1073 | 415 |

## 4.4 Dimensionless distance to the wall

Tab. 8 shows the dimensionless distance to the wall ($y^+$) of the first cell adjacent to the wall. ($y^+$) is shown in order to provide a measure of mesh size near the wall, that is, to know how the mesh is resolving the flow near the wall. In OpenFOAM notation it is yPlus. We show the global minimum (min), global average (avg) and global maximum (max). Additionally, we show the local minimum, local average and local maximum at the fully developed flow zone ($z = 4/5L$).

Table 8: Values of yPlus for different meshes

| **Mesh** | **Global** | | | **Local** | | |
|---|---|---|---|---|---|---|
| | **min** | **avg** | **max** | **min** | **avg** | **max** |
| Mesh10 | 2.1 | 3.3 | 3.9 | 2.1 | 3.2 | 3.8 |
| Mesh20 | 0.8 | 1.7 | 2.0 | 0.8 | 1.6 | 1.9 |
| Mesh40 | 0.3 | 0.8 | 1.0 | 0.4 | 0.8 | 1.0 |

### 4.5 Mesh sensitivity analysis

Taking into account the ITTC (International Towing Tank Conference) guidelines for uncertainty analysis in CFD verification and validation [ITTC, 2021], for our case the refinement ratio $r_i$ is 2. The solutions for the fine, medium and coarse mesh are $S_1$, $S_2$ and $S_3$ respectively. We take as reference the value of the Poiseuille number from Tab. 5. Therefore, the change between the medium and fine mesh is $\varepsilon_{21} = S_2 - S_1 = -0.39$. The change between the coarse and the medium mesh is $\varepsilon_{32} = S_3 - S_2 = -1.53$. The convergence ratio is $R_i = \varepsilon_{21}/\varepsilon_{32} = 0.2549$. This convergence ratio represents monotonic convergence, hence, generalized Richardson extrapolation can be used to estimate the error. The order of accuracy is $p_i = \ln(\varepsilon_{32}/\varepsilon_{21})/\ln(r_i) = 1.97$. The estimated error is $\delta = \varepsilon_{21}/(r_i^{p_i}) = -0.13$. Thus, the estimated solution is $S_C = S_3 - \delta = 56.90$ which is very close to the exact solution value of 56.91.

## 5 Discussion

As seen in Fig. 6, the simulation results in terms of kinematic pressure as a function of $z$ is very good. It behaves linearly and captures very well the slope and the total pressure drop [Bar-Meir, 2023, Shah and London, 1978]. As the simulation error of the pressure is of accumulative nature, we decided to plot the slope as a function of $z$ as shown in Fig. 7.

In Fig. 7, it is evident the error in the simulation results introduced by the inlet boundary condition. This error, although significant near the inlet, does not interfere downstream and lets us see how Mesh40 and the numerical schemes chosen are able to reproduce very well the fully developed flow analytical solution [Bar-Meir, 2023, Shah and London, 1978, Moharana and Khandekar, 2013].

Tab. 5 shows a detailed comparison of the pressure gradient, friction factor and Poiseuille number for the three meshes. There, it can be seen that Mesh40 produces the most accurate result with an error of just 0.25% with respect to the analytical solution obtained from Shah and London [1978]. This result is in agreement with Moharana and Khandekar [2013] as well for a big enough number of collocation points. Additionally, El-Genk and Pourghasemi [2019] focus on microchannels and microtubes, however, at least graphically, the Poiseuille number is between 55 and 60 for square section without slip which is in agreement with the results obtained in this work. Moreover, Syrjälä [1995] with another definition of the friction factor determine a value of 14.227077 for the Poiseuille number which converted to the definition used in this article is 56.908308 which is in agreement with our results. In addition, Barmak et al. [2024] with even another definition of the friction factor determine a value of 28.43 for the Poiseuille number which converted to the definition used in this article is 56.86 which is in agreement with our results. On the other hand, this result cannot be compared to Xu et al. [2000] because all their cross-sections are rectangular and none is the special case square. Furthermore, this result cannot be compared to Li et al. [2019] because they focus on the entrance length which is not the focus of this study.

The results and comparison of the velocity profiles are shown in Fig. 8 and Fig. 9. There, it can be seen that the velocity profiles of the simulation are in agreement with the analytical solution from Spiga and Morino [1994]. Obviously, Mesh40 offers the best spatial resolution and it reproduces more accurately the exact solution.

Notice that the velocity profile shown in Fig. 8 looks like the typical parabolic velocity profile found in circular cross-section pipes. But, the velocity profile in the diagonal cut shown in Fig. 9 is very different from a parabolic profile. That difference, at engineering level, reflects the difference in $w_{\max}/V$ and $f\mathrm{Re}$ for a circular cross-section pipe with respect to a square cross-section.

Tab. 6 shows the ratio $w_{\max}/V$. The ratio found for Mesh40 is 2.0898, which is very close to the analytical value of 2.0962 from Spiga and Morino [1994]. Additionally, the velocity ratio found in this work is in agreement with the value 2.1 found by Barmak et al. [2024]. On the other hand, Syrjälä [1995], Moharana and Khandekar [2013] and El-Genk and Pourghasemi [2019] did not report the velocity ratio for this case, therefore it cannot be compared.

As shown in Tab. 7, the time required to run the simulation is less than 1 minute for the two initial meshes (Mesh10 and Mesh20) but it required nearly 18 minutes for the finest mesh (Mesh40). In other words, the time required for Mesh40 is more than 22 times the time required for Mesh20. This is a huge jump in simulation time considering that the number of elements just increases by a factor of 4. On the other hand, the memory consumed is not high for any of the meshes considered and it is below 415MB. Finally, the memory required for Mesh40 is less than 3

times the memory required for Mesh20. This is below the expected 4 times increase in memory. This can be interpreted as OpenFOAM using optimal data structures internally.

Tab. 8 shows the values obtained for $y^+$ for all meshes. The global maximum value allows being sure that $y^+$ is below a certain target value i.e. $y^+ \leq 1.0$ [Pirozzoli and Orlandi, 2021]. This is an indicator that the whole simulation has an appropriate mesh size near walls. In addition, the local maximum value is an indicator that the mesh has a suitable size near walls in the zone of interest. For Mesh10, the local maximum $y^+$ is 3.8 and the error in terms of maximum velocity is 4.44%, whereas for Mesh40, the local maximum $y^+$ is 1.0 and the error reduces to 0.31%.

Finally, the mesh sensitivity analysis indicates monotonic convergence in terms of the Poiseuille number with respect to the mesh size. The order of accuracy attained is nearly 2. The estimated converged solution was 50.90 which is very close to the exact solution of 50.91.

As future work, the turbulent flow could be analyzed. Turbulent flow in square ducts is expected to behave in a similar way than in circular ducts with the respective changes in pressure drop and velocity profile as was seen in this work in the laminar case.

# 6 Conclusions

The application of OpenFOAM for simulating laminar flow in a square cross-section duct provides accurate results that align with theoretical predictions for a fine enough mesh. An excellent agreement was obtained between the computational solution and the analytical solution. It was confirmed that the Poiseuille number ($f\mathrm{Re}$) obtained computationally is equal to the analytical value of 56.91 within 0.25% margin. Furthermore, the ratio of maximum velocity to average velocity $w_{\max}/V$ is is equal to the analytical value of 2.0962 within a margin of 0.31%. Additionally, the velocity profile obtained computationally is in good agreement with the analytical velocity profile for both planes analyzed. It was shown that the velocity profile in a diagonal cut is not parabolic. Furthermore, it was determined that to accurately simulate this phenomena it is necessary to discretize the square section with around 40 elements per side, that is, 1600 quadrilateral elements in the entire cross section, although, even with 10 elements per side (100 quad elements in the cross-section) a fair accuracy is obtained. The case presented in this article serves for verification and validation in computational fluid dynamics and as a benchmark case for testing other computational fluid dynamics solvers or schemes. Finally, the results obtained with the mesh sensitivity analysis performed serve as a guide for mesh size definition in laminar incompressible internal flow.

For this case setup, the simulation time increases dramatically with the number of elements. Future work should focus on another setup in order to scale better when increasing the number of elements. Additionally, the inlet boundary condition should be improved in order to produce an inlet velocity profile more similar to the fully developed velocity profile.

# 7 Acknowledgements

Commented for blind review

# 8 Author contributions

Author: conceptualization, methodology, software, validation, visualization, writing (original draft, review and editing).

# 9 Conflicts of interest

The author declares no conflict of interest.

# 10 Data availability

The simulation case data is available on
https://github.com/espinozahg/square-duct-laminar-flow.

# References


N. Ashton and V. Skaperdas. Verification and validation of OpenFOAM for high-lift aircraft flows. *Journal of Aircraft*, 56(4):1641–1657, 2019. URL https://doi.org/10.2514/1.C034918.

G. Bar-Meir. *Basics of Fluid Mechanics*. Potto Project, 2023. URL https://zenodo.org/records/8184518.

I. Barmak, D. Picchi, A. Gelfgat, and N. Brauner. Flow of a shear-thinning fluid in a rectangular duct. *Physical Review Fluids*, 9(023303):1–15, 2024. ISSN 2469-990X. URL https://doi.org/10.1103/PhysRevFluids.9.023303.

K. Berry. *The TeX Live Guide*. TUG, 2023. URL https://www.tug.org/texlive/doc/texlive-en/texlive-en.html.

K. S. Bibin and J. S Jayakumar. Thermal hydraulic characteristics of square ducts having porous material inserts near the duct wall or along the duct centre. *International Journal of Heat and Mass Transfer*, 148(119079):1–17, 2020. ISSN 1879-2189. URL https://doi.org/10.1016/j.ijheatmasstransfer.2019.119079.

A. Downey. *Think Python*. Green Tea Press, 2015. URL https://greenteapress.com/thinkpython2/html/index.html.

M. S. El-Genk and M. Pourghasemi. Analytical and numerical investigations of friction number for laminar flow in microchannels. *ASME Journal of Fluids Engineering*, 141(3), 9 2019. ISSN 0098-2202. URL http://doi.org/10.1115/1.4041112.

O. A. González-Estrada, M. A. Rojas-Nova, and G. González-Silva. Effect of temperature on a vortex reactor for hydrodynamic cavitation. *Ingeniería e Investigación*, 42(3):1 – 7, 2022. ISSN 0120-5609. URL https://doi.org/10.15446/ing.investig.93419.

C. Greenshields. *OpenFOAM v11 User Guide*. The OpenFOAM Foundation, 2023. URL https://doc.cfd.direct/openfoam/user-guide-v11.

L. Huang, Y. Li, D. Benites-Muñoz, C. Windt, A. Feichtner, S. Tavakoli, J. Davidson, R. Paredes, T. Quintuna, E. Ransley, M. Colombo, M. Li, P. Cardiff, and G. Tabor. A review on the modelling of wave-structure interactions based on openfoam. *OpenFOAM Journal*, 2:116–142, 2022. ISSN 2753-8168. URL https://doi.org/10.51560/ofj.v2.65.

ITTC. *Uncertainty Analysis in CFD Verification and Validation*. International Towing Tank Conference, 2021.

S. Lain and A. D. Caballero. Analysis and discussion of two-way coupling effects in particle-laden turbulent channel flow. *Ingeniería e Investigación*, 43(1):1 – 12, 2023. ISSN 0120-5609. URL http://doi.org/10.15446/ing.investig.87275.

H. Li, B. Huang, and M. Wu. Experimental and numerical investigations on the flow characteristics within hydrodynamic entrance regions in microchannels. *Micromachines*, 10(5), 2019. ISSN 2072-666X. URL http://doi.org/10.3390/mi10050317.

X. Liu, J. Zhang, K. D. Nielsen, and Y. A. Cataño-Lopera. Challenges and opportunities of computational fluid dynamics in water, wastewater, and stormwater treatment. *Journal of Environmental Engineering*, 146(11), 2020. ISSN 1943-7870. URL https://doi.org/10.1061/(ASCE)EE.1943-7870.0001815.

Z. H. Liu, J. Wang, M. J. Ni, and N. M. Zhang. Unsteady mixed convection flows in a rectangular duct and dynamical behaviors of flow channel insert. *International Journal of Energy Research*, 2024(5510119):1–21, 2024. ISSN 1099-114X. URL https://doi.org/10.1155/2024/5510119.

M. F. Lumentut and M. I. Friswell. Powering smart pipes with fluid flow: effect of velocity profiles. *Computers & Structures*, 258:106680, 2022. ISSN 1879-2243. URL https://doi.org/10.1016/j.compstruc.2021.106680.

R.S.N. Mahmudah, R. Widiatmono, and D. Darmawan. The best setup for openfoamś buoyant cavity tutorial. *Journal of the Physical Society of Japan*, 92(12):124401, 2023. URL https://doi.org/10.7566/JPSJ.92.124401.

M. K. Moharana and S. Khandekar. Generalized formulation for estimating pressure drop in fully-developed laminar flow in singly and doubly connected channels of non-circular cross-sections. *Computer Methods in Applied Mechanics and Engineering*, 259:64–76, 2013. ISSN 0045-7825. URL http://doi.org/10.1016/j.cma.2013.03.005.

T. Neeraj, C. Velten, G. Janiga, K. Zähringer, R. Namdar, F. Varnik, and S. A. Hosseini. Modeling gas flows in packed beds with the lattice boltzmann method: validation against experiments. *Flow, Turbulence and Combustion*, 111(2):463–491, 2023. ISSN 1573-1987. URL https://doi.org/10.1007/s10494-023-00444-z.

H. Noriega, F. Guibault, M. Reggio, and R. Magnan. A case-study in open-source CFD code verification, part I: Convergence rate loss diagnosis. *Mathematics and Computers in Simulation*, 147:152–171, 2018. ISSN 0378-4754. URL https://doi.org/10.1016/j.matcom.2017.12.002.

NumPy Community. *NumPy User Guide*. NumPy Project, 2021. URL https://numpy.org/doc/1.21/user/index.html.

G. A. Orozco, C. T. González-Hidalgo, and F. Fajardo. Influence of agitator geometry in the dissolution kinetics of a spherical solid. *Ingeniería e Investigación*, 42(3):1 – 7, 2022. ISSN 0120-5609. URL https://doi.org/10.15446/ing.investig.94110.

S. Pirozzoli and P. Orlandi. Natural grid stretching for DNS of wall-bounded flows. *Journal of Computational Physics*, 439(110408):1 – 9, 2021. ISSN 1090-2716. URL https://doi.org/10.1016/j.jcp.2021.110408.

D. I. Quingatuña-Cali, J. E. Ramos-Peñafiel, and R. W. Pachacama-Choca. Estudio con dinámica de fluidos computacional de las arterias coronarias. *Polo del Conocimiento*, 7(7):2568–2585, 2022. ISSN 2550-682X.

J. D. Reina-Rozo and L. F. Medina-Cardona. Science, technology and solidarity: The emergence of a free culture for the future. *International Journal of Engineering, Social Justice, and Peace*, 8(1):86–104, 2021. ISSN 1927-9434. URL https://doi.org/10.24908/ijesjp.v8i1.14279.

A. Riaz, N. A. Ahammad, M. M. Alqarni, H. A. Hejazi, and E. M. Tag-ElDin. Peristaltic flow of a viscous fluid in a curved duct with a rectangular cross section. *Frontiers in Physics*, 10(961201): 1–12, 2022. ISSN 2296-424X. URL https://doi.org/10.3389/fphy.2022.961201.

O. O. Rodríguez-Díaz, E. Franco-Mejía, and E. Rosero. Modeling and control of small-scale underground mine ventilation networks. *Ingeniería e Investigación*, 43(1):1 – 8, 2023. ISSN 0120-5609. URL https://doi.org/10.15446/ing.investig.90968.

R. K. Shah and A. L. London. *Laminar Flow Forced Convection in Ducts*. Academic Press, 1978. URL https://doi.org/10.1016/C2013-0-06152-X.

A. Shingala, O. Cleynen, A. Jain, S. Hoerner, and D. Thevenin. Genetic optimisation of a free-stream water wheel using 2D computational fluid dynamics simulations points towards design with fully immersed blades. *Energies*, 15(10):3723, 2022. ISSN 1996-1073. URL https://doi.org/10.3390/en15103723.

M. Spiga and G. L. Morino. A symmetric solution for velocity profile in laminar flow through rectangular ducts. *International Communications in Heat and Mass Transfer*, 21(4):469–475, 1994. ISSN 0735-1933. URL http://doi.org/10.1016/0735-1933(94)90046-9.

S. Syrjälä. Finite-element analysis of fully developed laminar flow of power-law non-Newtonian fluid in a rectangular duct. *International Communications in Heat and Mass Transfer*, 22(4): 549–557, 1995. ISSN 0735-1933. URL http://doi.org/10.1016/0735-1933(95)00040-6.

E. Troger, N. Treleaven, F. Laniz, C. Wendling, and M. Brush. *Geany: a fast, light, GTK+ IDE*. Geany contributors, 2023. URL https://www.geany.org/manual/current/index.html.

J. A. Wheeler and E. H. Wissler. The friction factor - Reynolds number relation for the steady flow of pseudoplastic fluids through rectangular ducts: Part I. Theory. *AIChE Journal*, 11(2): 207–212, 1965. ISSN 0045-7825. URL http://doi.org/10.1002/aic.690110208.

T. Williams and C. Kelley. *gnuplot 5.4: An interactive plotting program*. gnuplot team, 2022. URL http://www.gnuplot.info/docs_5.4/Gnuplot_5_4.pdf.

B. Xu, K.T. Ooti, N.T. Wong, and W.K. Choi. Experimental investigation of flow friction for liquid flow in microchannels. *International Communications in Heat and Mass Transfer*, 27(8): 1165–1176, 2000. ISSN 0735-1933. URL http://doi.org/10.1016/S0735-1933(00)00203-7.

W. Zhang, J. Calderon-Sanchez, D. Duque, and A. Souto-Iglesias. Computational fluid dynamics (CFD) applications in floating offshore wind turbine (FOWT) dynamics: A review. *Applied Ocean Research*, 150:104075, 2024. ISSN 1879-1549. URL https://doi.org/10.1016/j.apor.2024.104075.

Y. A. Çengel and J. M. Cimbala. *Fluid Mechanics*. McGraw-Hill, 2018.